Journal of
Synchrotron
Radiation

ISSN 0909-0495

Received 22 August 2011
Accepted 4 December 2011

A desktop X-ray monochromator for synchrotron radiation based on refraction in mosaic prism lenses

Tao Liu,[a]* Rolf Simon,[a] David Batchelor,[a] Vladimir Nazmov[b] and Michael Hagelstein[a]

[a]Institute for Synchrotron Radiation, Karlsruhe Institute of Technology, D-76344 Eggenstein-Leopoldshafen, Germany, and [b]Institute of Microstructure Technology, Karlsruhe Institute of Technology, D-76344 Eggenstein-Leopoldshafen, Germany. E-mail: tao.liu@kit.edu

Focusing planar refractive mosaic lenses based on triangular prism microstructures have been used as an alternative approach for wide-bandpass monochromatization of high-energy X-rays. The strong energy dependence of the refractive index of the lens material leads to an analogous energy dependence of the focal length of the lens. The refractive mosaic lens, in comparison with the refractive lens of continuous parabolic profile, is characterized by a higher aperture because of reduced passive material. In combination with a well defined pinhole aperture in the focal plane, the transmittance of photons of an appropriate energy can be relatively high and photons of deviating energy can be efficiently suppressed. The photon energy can be tuned by translating the pinhole along the optical axis, and the bandwidth changed by selecting appropriate pinhole aperture and beam stop. This method of monochromatization was realised at the ANKA FLUO beamline using a mosaic lens together with a 20 μm pinhole and beam stop. An energy resolution of 2.0% at 16 keV has been achieved.

Keywords: X-ray optics; refractive mosaic lens; monochromator.

1. Introduction

A monochromator or wavelength selector operates either by refraction at the boundaries of a prism or diffraction using a grating or crystal, to spatially separate light of different wavelength. Both approaches have in common that light of a chosen wavelength is extracted by placing an exit slit at a suitable position. At photon energies in the hard X-ray regime, monochromators made of a pair of crystals or multilayer mirrors are widely used for synchrotron radiation beamlines which can provide an energy bandwidth of typically 10^{-4} and 10^{-2}, respectively. The double multilayer monochromator (DMM) has become popular in newly built synchrotron radiation beamlines in recent years because it can provide higher flux than crystal monochromators, a moderate energy resolution, and can be used for high-energy X-rays up to $\sim$40 keV (Kazimirov *et al.*, 2006).

As important optical elements, compound refractive lenses (CRLs) have intensively been used for optical focusing of hard X-rays at synchrotron radiation facilities (Snigirev *et al.*, 1996; Lengeler *et al.*, 1999; Aristov *et al.*, 2000; Cederström *et al.*, 2000, 2002, 2005; Jark *et al.*, 2004, 2006, 2008; De Caro & Jark, 2008). Compared with other focusing elements, CRLs present several attractive features. They are straightforward to align, relatively insensitive to misorientations (Andrejczuk *et al.*, 2010) and interface roughness, do not alter the beam propagation direction and can be adapted to up to 100 keV photon energy (Nazmov *et al.*, 2005). A spot size down to around 50 nm has been reported using a synchrotron radiation undulator source (Schroer *et al.*, 2005). The focal length of a CRL depends on photon energy because of the strong energy dispersion of the refractive index of the CRL material. Though this chromatic aberration hampers the suitability of the CRL for focusing polychromatic light, it can be exploited for monochromatization. If the lens is operated in conjunction with a well defined pinhole aperture in the image plane, only photons of a certain energy and bandwidth will pass through the pinhole. Photons with deviating energy have a different focus and consequently a small throughput. Tuning the energy can be achieved by the longitudinal translation of the pinhole along the optical axis. This concept of a lens–pinhole combination makes it possible to employ as an energy filter or wide-bandpass monochromator. A significant advantage of this concept is that the direct rays from the light source do not change their propagation direction and consequently there is no lateral offset. Thus focusing (or collimating) and dispersion of X-rays can be integrated in a single instrument.

Energy filters based on refractive X-ray lenses have been shown to improve energy resolution and thereby lower the dose for medical imaging applications (Fredenberg *et al.*, 2008; Jark, 2004). The chromatic nature of the X-ray focusing lenses has also been explored by using a vacuum-compatible CRL

component installed at the undulator beamline ID11 at ESRF. The X-ray energy and the focal length can be varied continuously throughout a large range of energies and distances by changing the number of lenses inserted into the beam path, and it can be used as an extremely high flux broad-bandpass monochromator aligned to the energy generated by an undulator as an X-ray source (Vaughan *et al.*, 2011).

In this work a large aperture mosaic prism X-ray lens has been used for realising an X-ray refractive monochromator (XRM). The comparatively large aperture and large beam divergence of this lens was expected to result in a large photon throughput and a tunable energy bandwidth. The experimental XRM was realised at the bending-magnet beamline FLUO at ANKA (Simon *et al.*, 2003) and has achieved a 2% energy bandwidth at a photon energy of 16 keV. In principle, polymer X-ray lenses can offer a range of monochromatization from 5 keV to 100 keV photon energy. Possible applications of the XRM at synchrotron radiation beamlines span from microfluorescence analysis to hard X-ray microscopy and full-field X-ray imaging.

2. Experiment

The planar mosaic X-ray prism lenses (XPLs) for this investigation were developed and made using the LIGA technique at the Institute of Microstructure Technology, Karlsruhe Institute of Technology (Nazmov *et al.*, 2004). The XPLs were made of SU-8, a highly sensitive negative photoresist. It is almost transparent to high-energy X-rays, and is very stable against radiation damage. No radiation damage was observed in a white radiation beam during two weeks in the bending-magnet beamline FLUO at ANKA when metal foils (filters) were used to block out the unused low-energy part of the spectrum. It was found that natural cooling through air convection and thermal conduction through the silicon substrate were sufficient to remove the deposited heat load. In the case of a high-power insertion-device light source, such as a wiggler source, water cooling of the substrate may be necessary or a substrate made of copper may be sufficient (Nazmov *et al.*, 2007). The XPLs used for this investigation of monochromatization were optimized at 15.8 keV and are characterized by a large geometric aperture, 2.9 mm, with a transparency of 0.44, resulting in an effective aperture of 1.27 mm (Nazmov *et al.*, 2012). The micrographic sections of the XPLs are shown in Fig. 1. The mosaic patterns are made of a regular stack of many separate or attached symmetric prism segments deposited on the surface of a silicon wafer with a height of 100 µm. The triangular cross section of each prism segment at the entry of the XPL is 31 µm wide at the base, 12 µm in height (h) and has a tilt angle of 38° (φ), as shown in Fig. 1(c).

The lens was designed for one-dimensional X-ray focusing. For a single prism segment, the beam deviation, Δ, caused by the refraction is rather small and is given by Snell's law (Born & Wolf, 1980),

$$\Delta = 2\delta/\tan\varphi, \qquad (1)$$

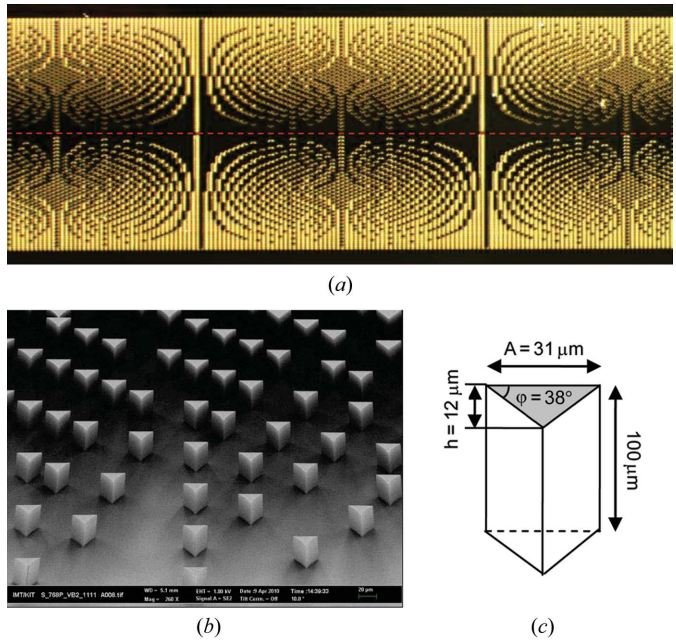

(a) (b) (c)

Figure 1
(a) Section (top view) of the optical micrograph of a mosaic prism lens made using the lithography technique; the lens is made of an arrangement of many prisms with triangular cross section (made of SU8), shown as grey spots (yellow online), deposited on a silicon substrate. The prism segments are symmetrically arranged in lateral dimension on the two sides of the optical axis. The lateral size of the lens is 2.9 mm and the longitudinal length is 30 mm. The optical axis is indicated by a dashed line. It was designed for one-dimensional focusing with 2.9 mm geometric aperture in focal dimension; the other dimension was limited to 100 µm by the height of prism segments. (b) A small section near the optical axis was observed by scanning electron micrograph showing individual prism segment with triangular cross section. (c) The dimensions of a prism segment at the entry of the lens aperture are shown.

where φ is the incident angle which is equal to the tilt angle of the triangle segment and δ is the refractive index decrement of the lens material. If we assume no change of propagation direction along the lens (short lens approximation), this leads to the common refractive focal length for the Mth row in the structure,

$$f = \frac{Mh}{\Delta NM} = \frac{h\tan\varphi}{2N\delta}, \qquad (2)$$

where N is the number of prisms in the first row. The mosaicity was designed such that the laterally refracted beam should have a common focal plane. The number of prisms per row increases with increasing distance from the optical axis, as shown by the central dashed line in Fig. 1. To achieve a focal distance of 525 mm at 16 keV, a total length of 30 mm was used for the XPL. In both the present design and in the design of classidra (Jark *et al.*, 2004), a refractive prismatic microstructure with triangular cross section has been employed. However, compared with the 'thin' lens design of classidra, every prism microstructure is arranged along the X-ray propagation direction in the lens. Hence, the lens was made adiabatically according to the long lens propagation (Nazmov *et al.*, 2012). The geometric aperture of the lens varies slightly from entrance to exit, and the dimensions of the triangular cross section of prism segments are also changed slightly over

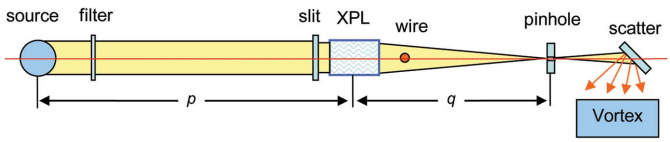

Figure 2
Schematic layout of the X-ray refractive monochromator set-up installed at the FLUO beamline. From left to right, the coaxial components are: bending-magnet source, filter, four-blade entrance slit, mosaic prism lens, single tungsten wire, pinhole, metal foil reference and scatter sample, and an energy-resolved detector (Vortex). The XPL is used for vertical focusing here.

the whole lens. Moreover, the SU8 resist was known to be more resistant to radiation than the material Plexiglas used for clessidra (Khan Malek, 2002). The rigidity of the structure was guaranteed by a high-precision LIGA technique. The present XPL is also different from the rolled X-ray prism lens, which is made by rolling structured polyimide film and used for two-dimensional focusing (Simon *et al.*, 2010; Vogt *et al.*, 2011).

The XRM is schematically illustrated in Fig. 2. The XPL was hosted by a motorized stage with five degrees of freedom (three translations and two rotations) which was mounted at a distance p = 12 m from the source. The white-beam radiation from the bending-magnet source, with a critical energy of 6.25 keV, propagates through an aluminium filter (250 µm thick) and by-passes a multilayer monochromator in the beamline. The filter acts as a high-energy bandpass reducing heat load and radiation dose on the XPL; its cut-off energy is below the operation range of the monochromator. The entrance slit in front of the lens confines the beam profile illuminating the lens to 0.10 mm (horizontal) × 2 mm (vertical), matching the aperture of the XPL. At 16 keV the lens produced an image of the source at a working distance q = 0.550 m. The vertical focus spot size was measured to be 10.8 ± 0.5 µm using a CCD camera (pixel size of 0.55 µm). The energy resolution of the XRM was varied by changing the size of the exit aperture and by blocking the central part of the beam transmitted through the XPL. The aperture consisted of an array of platinum top-hat pinholes with sizes of 20, 30, 50 and 100 µm (Plano GmbH), and was mounted on a separate stage consisting of two rotations and three translations. Tungsten wires with different diameters were used as beam stops to block the central part of the beam transmitted through the XPL. The energy bandwidth was measured either with an energy-dispersive detector or with a channel-cut monochromator and PIN diode. Since the energy-dispersive detector would not withstand the photon flux of the direct beam, the radiation scattered by a metal foil behind the pinhole was measured. Heavy metals like silver and indium were used because the largest part of the radiation is scattered elastically and K or L fluorescence peaks are beyond the energy range of interest. An energy-resolved silicon drift diode detector (Vortex) was used to record the energy spectra containing scattering and fluorescence components. The energy resolution of the detector was 205 eV at 16 keV.

The alternative set-up for measuring the energy resolution of the XPL-based XRM consisted of a channel-cut crystal (Si 111) replacing the scattering foil. The diffracted beam intensity from the channel-cut crystal was measured using a photodiode mounted further downstream.

Table 1
Input parameters for the wavefront propagation simulation using a compound refractive lens at the ANKA FLUO beamline; some data from calculation at a photon energy of 16 keV are also listed.

Full geometric aperture	600 µm
Radius at apex	100 µm
Number of lenses	100
Total lens length	91 mm
Space between apexes	10 µm
Lens material	PMMA
Focal distance	0.48 m
Focus depth	0.50 mm
Image distance	0.50 m
Effective aperture	286 µm
Intensity transmission	9.0%

3. Simulation

Optical simulations were performed using the wavefront computation code *SRW* (Chubar & Elleaume, 1998) on a parabolic CRL. The code presents a near-field treatment of the X-ray wavefront propagation from an electron beam travelling through various magnetic fields and to an observation spot in a plane located at some distances from the source. A set-up is simulated using a parabolic CRL for vertical focusing which is installed at the FLUO beamline, as shown in Fig. 2 (the XPL was replaced by a CRL made of PMMA). Whilst the CRL is not exactly the same as an XPL, the intrinsic physics is the same, and the results can demonstrate well the effect of some parameters of the XRM. The parameters of the CRL are listed in Table 1. The lens is vertically configured at p = 12 m from the bending-magnet source, producing an image size of 33.3 µm (horizontal) × 8.33 µm (vertical) at q = 0.5 m. The propagation of X-rays along the longitudinal axis is confined by an entrance slit which is located at 11.8 m from the source with a 0.1 mm (horizontal) × 0.6 mm (vertical) aperture. Horizontally aligned wires placed on the optical axis

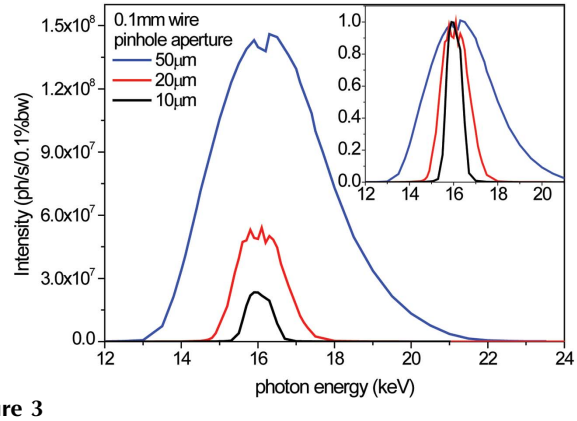

Figure 3
Calculated photon flux through the pinhole as a function of photon energy with the following configuration: bending-magnet source, slit, CRL, 0.1 mm wire, pinhole. The transmitted fluxes for 50, 20 and 10 µm aperture pinholes have been simulated. The inset re-plots the curves by normalizing to the maximum peaks.

were used as beam stops. At the focus of the lens, a circular pinhole is used to select X-rays of certain wavelength. The flux passing through the pinhole was calculated as a function of X-ray photon energy.

Fig. 3 shows a plot of the calculated photon flux as a function of photon energy at various pinhole apertures and with a 0.1 mm-diameter wire as beam stop. The normalized spectra are plotted in the inset. The energy resolution, estimated from the peak width, is strongly improved with reduced pinhole apertures. The dependence is almost linear and confirmed by the experiments shown later. Fig. 4 shows the photon fluxes through the 20 µm pinhole without a wire and with 0.1 and 0.3 mm wires as beam stops. It is seen that the energy bandwidth is also sensitive to the beam-stop size. The long tails at both sides of the peaks can be effectively removed by using the beam stop, at the cost of the total photon flux. Fig. 5 shows the results for the three geometric aperture pinholes (200, 400 and 600 µm) while using a 0.1 mm wire, a 20 µm pinhole and keeping all the other parameters of CRL the same. Accordingly, the effective apertures increase to 175, 254 and 268 µm. The higher effective aperture has a higher throughput, hence a sharper energy bandwidth. The simulations also indicated that the pinhole can be replaced with a two-blade slit in the case of one dimensional focusing, with comparable energy resolution but much increased photon flux throughput.

4. Performance test

Fig. 6 shows the elastic scattering peaks from the scatter samples (indium and silver metal foils) measured by the Vortex detector at various distances between pinhole and XPL. Since elastic scattering does not change photon energy, the elastic peak energy corresponds to the photon energy filtered by the pinhole (spikes owing to Bragg diffraction peaks are visible in the silver foil spectra). The energy can be tuned from 12 to 20 keV by moving the pinhole from 285 to

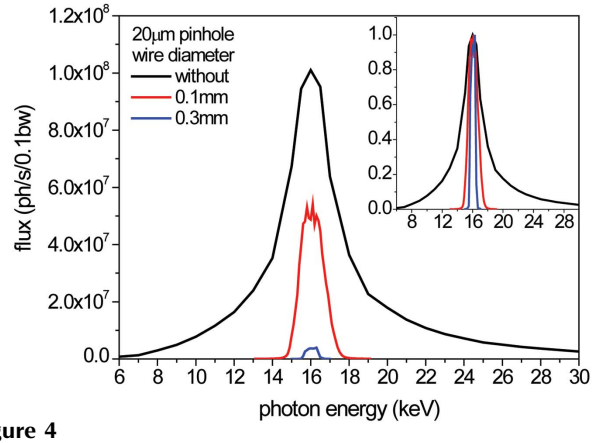

Figure 4
Calculated photon flux transmitted through a 20 µm pinhole as a function of photon energy with the following configuration: bending-magnet source, slit, CRL, wire (without a wire, 0.1 or 0.3 mm-sized wires), pinhole. The wires are horizontally configured on the optical axis. The inset re-plots the transmitted fluxes by normalizing to the maximum peaks.

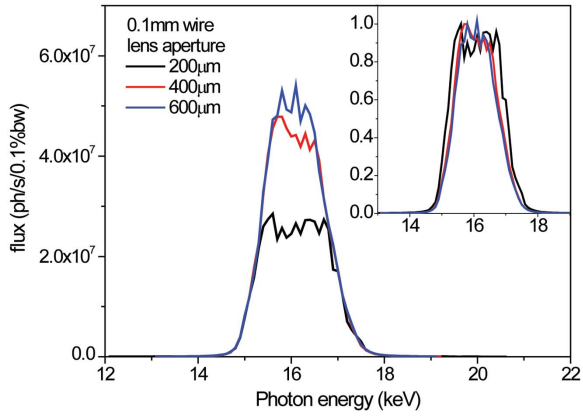

Figure 5
Calculated photon flux transmitted through a 20 µm pinhole as a function of photon energy with the following configuration: bending-magnet source, slit, CRL with 200, 400 and 600 µm apertures, 0.1 mm wire, pinhole. The wires are horizontally configured on the optical axis. The inset re-plots the transmitted fluxes by normalizing to the maximum peaks.

925 mm. The inset is a plot of the filtered photon energy as a function of the longitudinal distance from the lens, fitted by the function: distance [mm] = 2.08 × $10^{-6}E^2$ [eV]. The quadratic dependence is expected as, from equation (2), $f \propto \delta^{-1}$ and $\delta \propto E^{-2}$, where E is the photon energy. The energy dependence of the XPL is stronger compared with other focusing elements, such as Fresnel zone plates and Kirkpatrick–Baez mirrors (Snigirev & Snigireva, 2008).

Fig. 7 shows the elastic scattering peaks at 15.7 keV from the indium foil measured with a 20 µm pinhole aperture, and varying diameters of the tungsten wire used as central beam stop (0.25, 0.6 and 1.0 mm-diameter wires and without a wire), using the XRM under broadband synchrotron radiation. The configuration for DMM is a combination of the double

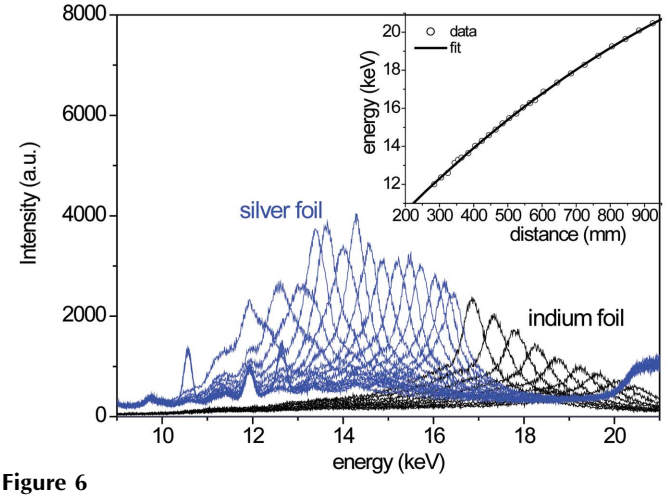

Figure 6
Elastic-scattering peaks from the scatter sample (silver or indium metal foil) measured by an energy-resolved detector with the following optical configuration: white beam, XPL, 20 µm pinhole, scatter sample. The pinhole was displaced at a variety of distances from the lens. The inset shows a plot of the energy position (keV) of the elastic-scattering peaks as a function of the lens distance. A polynomial function of order 2 was fitted to the photon energy.

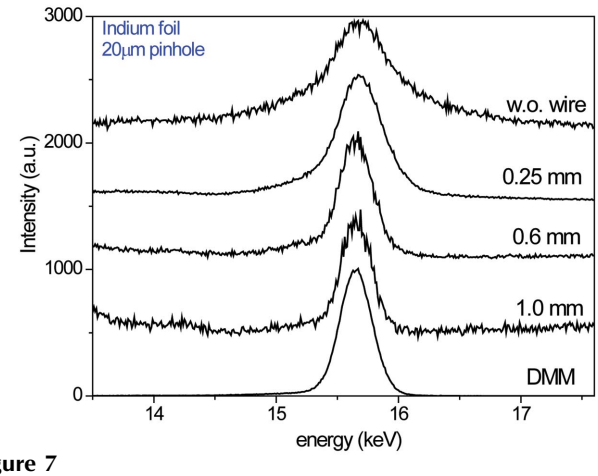

Figure 7
Elastic-scattering peaks from an indium foil sample measured by the energy-resolved detector with the following optical configuration: white beam, XPL, without a wire and with 0.25, 0.6, 1.0 mm wires, 20 μm pinhole, scatter sample; DMM (white beam, double multilayer monochromator, XPL, scatter sample). The intensity was normalized to the peak maximum.

multilayer monochromator with the lens. Consistent with the simulations, it is seen that a much improved resolution was achieved by inserting the wire, as estimated by the FWHM (full width at half-maximum) values of the elastic-scattering peaks, which are 626 eV (without a wire), 418 eV (0.25 mm), 319 eV (0.6 mm), 288 eV (1.0 mm) and 309 eV (DMM). If we neglect the intrinsic instrumental broadening of the detector, these correspond, respectively, to 4.0%, 2.7%, 2.0%, 1.8% and 2.0% bandwidths. The optimized 1.8% bandwidth obtained by the XRM is clearly comparable with that of a standard DMM. Fig. 8 shows the elastic-scattering peaks at 15.7 keV from the indium foil at 20, 30, 50 and 100 μm pinhole aperture, and in the absence of a wire. As predicted, the resolution was improved significantly by using smaller pinholes. A linear dependence is seen in the inset.

The energy resolution can be further estimated by measuring the diffraction using a channel-cut crystal mounted

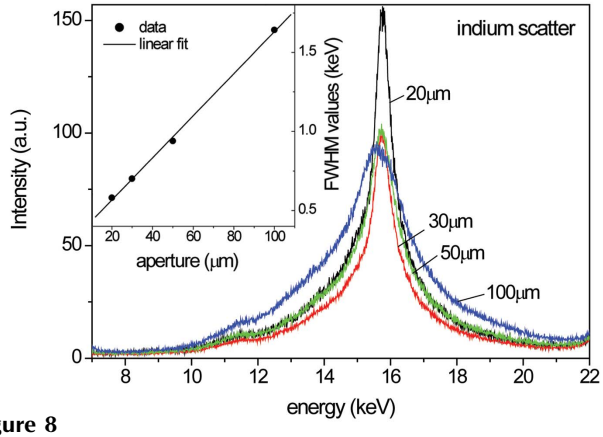

Figure 8
Elastic-scattering peaks from indium foil measured using the energy-resolved detector, using different aperture pinholes with the following optical configuration: white beam, XPL, pinhole, scatter sample; in the absence of a beam stop. The inset shows the FWHM data and a linear fit at various pinhole apertures.

at a distance of 520 mm from the XPL. Based on Bragg's law, in equation (3), the energy resolution, $\Delta E/E$, is determined by the angular dispersion, $\Delta\theta$, of the diffracted beam, where θ_0 is the Bragg angle. $\Delta\theta$ consists of three parts: the true energy bandwidth of the incident beam (ω_E); the geometric instrumental divergence seen by the crystal which includes the angular beam dispersion (ω_{geom}) of the incident beam and the source size (ω_S); the intrinsic Darwin width of the crystals (assuming no crystal defects, ω_D) (Sánchez del Río, 1998),

$$\Delta E/E = \Delta\theta \cot\theta_0 = \left[\omega_E^2 + \left(\omega_{geom} + \omega_S\right)^2 + \omega_D^2\right]^{1/2} \cot\theta_0. \quad (3)$$

With a vertically focusing configuration of the XRM at the FLUO beamline, the vertical source size is 0.2 mm. The estimated values of ω_S and ω_D at 16 keV are 0.017 mrad and 0.024 mrad, respectively; therefore, the angular dispersion (ω_{geom}) of the focused beam from the XPL dominates in (3). It varies from 7.5 mrad to 1.9 mrad as the pinhole translates from 0.2 m to 0.8 m along the optical axis. To avoid this large angular dispersion influencing the bandwidth measurements, the XPL was mounted horizontally for horizontal focusing and the channel-cut crystals were mounted vertically; the entrance slit was confined to 1.5 mm (horizontal) × 0.1 mm (vertical). In this way the vertical angular dispersion of the incident beam seen by the crystals is 0.077 mrad, which is the vertical divergence of the beamline and, being much smaller than ω_E, can therefore be ignored (hence $\Delta\theta \simeq \omega_E$). The flux transmitted through the XPL, configured with a 20 μm pinhole and various beam stops (without a wire, with 0.25, 0.6 and 1.0 mm wires), was analyzed by the channel-cut crystal. The diffraction peaks of Si 111 are shown in Fig. 9. The energy bandwidth, ω_E, is calculated as 5.8%. 4.5%, 3.6% and 2.0%, respectively. Higher background is seen for the curves without or with thinner beam stops.

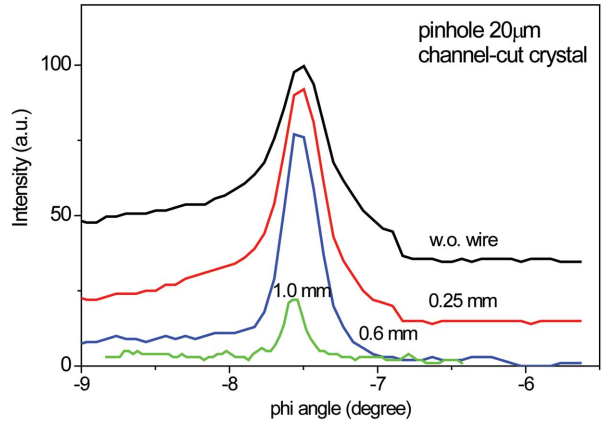

Figure 9
Rocking curves of Si 111 diffraction from a channel-cut crystal measured with a 20 μm pinhole and at various beam stops (wire): without a wire, with 0.25 mm, 0.6 mm and 1.0 mm wires. The lens was horizontally configured and the channel-cut crystals were vertically configured. The optical configuration of the XRM is white beam, XPL, wires (with or without), pinhole, channel-cut crystals.

5. Discussion

The photon intensity passing through the XRM can be compared with that of a DMM. Because of the built-in lens focusing, it is obvious that the XRM delivers brighter monochromated radiation at the focus position, and the brightness is specified by the gain of the lens. In the case of the DMM used in combination with a lens, the intensity passing through the monochromator is determined by the reflectivity of the multilayers and the gain of the lens. Assuming the same transmission and the same acceptance aperture for the lens, the decreased beam intensity in XRM is mainly because of the beam-stop attenuation. Fig. 10 shows the relative flux intensity at 16 keV, after the white beam propagating through a slit at 11.5 m and a central one-dimensional obstruction (wire) placed at 11.9 m at the FLUO beamline, calculated using the ray-tracing code *Shadow* (Welnak *et al.*, 1994). The calculations were performed for two slit openings: (i) 0.1 mm (horizontal) × 1.5 mm (vertical), wire horizontal; (ii) 1.5 mm (horizontal) × 0.1 mm (vertical), wire vertical. It is seen that the flux intensity reduces to about half at the obstruction size of 0.6–0.7 mm. This efficiency of the XRM may be comparable with that of a DMM, considering the multilayer reflectivity and interface roughness in the latter.

In a previous work the energy filtering properties of a prism-array lens were explored in a polychromatic beam (Jark, 2004). The energy bandwidth was analyzed theoretically based on the field-propagation model and was found to be inversely proportional to the intensity gain of the lens. With a geometric aperture of 194 µm and a total length of 9 mm, the filter exhibited a 29% energy bandwidth as tested at a bremsstrahlung set-up (Jark, 2004). Similarly, a planar parabolic CRL has been tested in our experiments at the FLUO beamline. The used CRL is featured with 320 µm geometric aperture, 20 µm curvature radius, number of lenses N = 18, and 0.52 m working distance at 15.8 keV. Depending on the different beam stops and pinhole apertures, 18–30% bandwidths were obtained at 16 keV. It is almost one order of magnitude higher than that of the XPL. This is a clear indication that a large lens aperture is crucial for achieving high energy resolution, which can easily be illustrated: a lens of larger numerical aperture has a shallower depth of field; therefore, energies will be more highly localized longitudinally, producing a narrower bandwidth for the filtered beam by the pinhole. The XPL made particularly for this purpose is featured with large geometric aperture (2.9 mm) because of the novel mosaicity design.

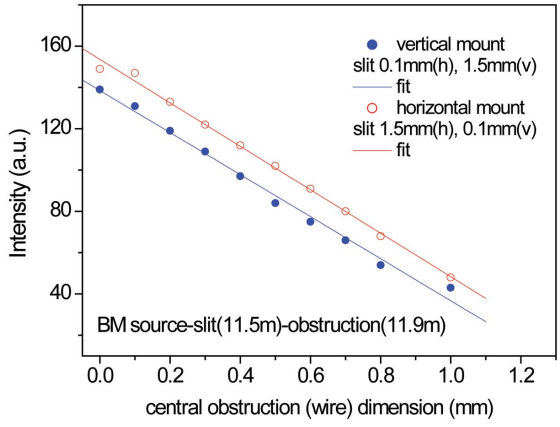

Figure 10
Relative intensity of the X-ray beam from the bending-magnet source, passing through a slit which is configured vertically or horizontally, and with an obstruction (wire) with varying diameters; the calculation was performed using a ray-tracing code at the FLUO beamline. The data were fit by linear functions. The selection of different beam stops (obstruction) corresponds to a varying energy bandwidth of the XRM.

The monochromatic beam obtained by the XRM can be used for various types of experiments with a sample placed on the optical axis. A critical point for practical applications is that the beam is highly divergent in one dimension because of the focus created by the XPL. If a small probing beam size is required, the sample has to be placed very close to the pinhole or a refocusing element must be installed behind the pinhole to create a second focus. Some applications may not even require a pinhole at the focal plane, *e.g.* when a sample smaller than the focused beam is placed in the focal point or when a suitable spatially resolving detector is used. Although the XRM may not be the best choice when very high energy resolution and low beam divergence are demanded, it may be a very interesting option when high flux, intensity and tunable bandwidth are required. Since the monochromatization is based on refraction, there are no higher-order components (and also glitches) in the monochromated beam, so additional devices or efforts for suppressing higher harmonic are not required. The conventional double-crystal or multilayer monochromators usually have fixed-energy bandwidth at a certain photon energy; the bandwidth can be changed only by the exchange of crystals or multilayer mirrors. Certain regions of energy bandwidth are difficult to obtain, and the DMM shows strong absorption above the K, L edges of the materials used. In contrast, the energy resolution or bandwidth of XRM can be simply tuned by selecting appropriate pinholes and beam stop.

In a more elaborate set-up, pinhole and wire can be exchanged with several pairs of slits, like the Young slits of varying width, and placed at various distances from the lens, providing different energies. Since the XRM may contain a significant high-energy background component if it is used for broadband sources, such as bending-magnet or wiggler sources, an effective beam stop and proper radiation shielding is crucial. A thick pinhole wall is also necessary because the filtered monochromatic beam may be dominated by the transmitted high-energy background components.

In the XRM the front slit must match the lens aperture; the limited acceptance aperture of the lens determines the efficiency. The above simulations for CRLs have shown that the effective aperture significantly affects the energy resolution. Similarly it has also been shown in a theoretical evaluation by Jark (2004) that a lens with large aperture is very critical for achieving high flux and high energy resolution at the focus. The efficiency of the present XPL is limited by the 100 µm height of the prism segments in one dimension. It can be improved by using lenses with larger heights or by two-

dimensional focusing using two sets of orthogonally configured lenses or one set of the cross lenses (Nazmov *et al.*, 2004).

The developed XRM can be applied to experiments such as X-ray microfluorescence analysis and hard X-ray microscopy and imaging. X-ray microscopy can profit from the possibility of the hollow conical illumination of the object. Scattering from the small-aperture pinhole can be reduced by using a second aperture behind. As the refractive lens is used for hard X-ray focusing, and can be used up to 100 keV photon energy, all components can work in air. For very high photon energy applications, lenses made of other materials, such as nickel, can be adopted (Nazmov *et al.*, 2005).

6. Conclusions

A desktop set-up for X-ray monochromatization, combining X-ray mosaic-arranged lenses with focusing elements of triangular cross section and pinhole, was developed at the FLUO beamline, ANKA. The XRM makes use of the chromaticity of refractive lenses in white-beam radiation. The lens, beam stop and pinhole aperture are subsequently mounted along the optical axis, and each can be aligned with the necessary degrees of freedom. The photon energy can be tuned by longitudinally translating the pinhole along the optical axis. It provides the capability of simultaneously monochromatizing as well as focusing of the X-ray beam. The simulation and experimental results have shown that the energy resolution can be significantly improved by using a large-aperture lens, small pinhole apertures and a beam stop in the beam path. An optimal 2.0% bandpass has been demonstrated at a photon energy of 16 keV, which is comparable with that of a standard DMM. The energy resolution or bandwidth can be simply changed by selecting pinhole aperture and beam stop.

We would like to thank Gerhard Grübel (DESY) for supplying a precision pinhole and Patrick Vagovic (KIT) for the provision of a channel-cut Si monochromator. We also thank Anton Plech (KIT) for useful comments on the manuscript.

References

Andrejczuk, A., Krzywiński, J., Sakurai, Y. & Itou, M. (2010). *J. Synchrotron Rad.* **17**, 616–623.

Aristov, V. V., Grigoriev, M. V., Kuznetsov, S. M., Shabelnikov, L. G., Yunkin, V. A., Hoffmann, M. & Voges, E. (2000). *Opt. Commun.* **177**, 33–38.

Born, M. & Wolf, E. (1980). *Principles of Optics.* Oxford: Pergamon Press.

Cederström, B., Cahn, R. N., Danielsson, M., Lundqvist, M. & Nygren, D. R. (2000). *Nature (London)*, **404**, 951.

Cederström, B., Lundqvist, M. & Ribbing, C. (2002). *Appl. Phys. Lett.* **81**, 1399–1401.

Cederström, B., Ribbing, C. & Lundqvist, M. (2005). *J. Synchrotron Rad.* **12**, 340–344.

Chubar, O. & Elleaume, P. (1998). *Proceedings of the Sixth European Particle Accelerator Conference (EPAC98)*, Stockholm, Sweden, 22–26 June 1998, pp. 1177–1179.

De Caro, L. & Jark, W. (2008). *J. Synchrotron Rad.* **15**, 176–184.

Fredenberg, E., Cederström, B., Åslund, M., Ribbing, C. & Danielsson, M. (2008). *X-ray Opt. Instrum.* **2008**, 1–8.

Jark, W. (2004). *X-ray Spectrom.* **33**, 455–461.

Jark, W., Matteucci, M. & Menk, R. H. (2008). *J. Synchrotron Rad.* **15**, 411–413.

Jark, W., Pérennès, F. & Matteucci, M. (2006). *J. Synchrotron Rad.* **13**, 239–252.

Jark, W., Pérennès, F., Matteucci, M., Mancini, L., Montanari, F., Rigon, L., Tromba, G., Somogyi, A., Tucoulou, R. & Bohic, S. (2004). *J. Synchrotron Rad.* **11**, 248–253.

Kazimirov, A., Smilgies, D.-M., Shen, Q., Xiao, X., Hao, Q., Fontes, E., Bilderback, D. H., Gruner, S. M., Platonov, Y. & Martynov, V. V. (2006). *J. Synchrotron Rad.* **13**, 204–210.

Khan Malek, C. (2002). *Microelectron. J.* **33**, 101–105.

Lengeler, B., Schroer, C., Tümmler, J., Benner, B., Richwin, M., Snigirev, A., Snigireva, I. & Drakopoulos, M. (1999). *J. Synchrotron Rad.* **6**, 1153–1167.

Nazmov, V. *et al.* (2012). In preparation.

Nazmov, V., Reznikova, E., Last, A., Mohr, J., Saile, V., DiMichiel, M. & Göttert, J. (2007). *Nucl. Instrum. Methods Phys. Res. A*, **582**, 120–122.

Nazmov, V., Reznikova, E., Snigirev, A., Snigireva, I., DiMichiel, M., Grigoriev, M., Mohr, J., Matthis, B. & Saile, V. (2005). *Microsyst. Technol.* **11**, 292–297.

Nazmov, V., Reznikova, E., Somogyi, A., Mohr, J. & Saile, V. (2004). *Proc. SPIE*, **5539**, 235–243.

Sánchez del Río, M. (1998). *Proc. SPIE*, **3448**, 230–245.

Schroer, C. G., Kurapova, O., Patommel, J., Boye, P., Feldkamp, J., Lengeler, B., Burghammer, M., Riekel, C., Vincze, L., van der Hart, A. & Küchler, M. (2005). *Appl. Phys. Lett.* **87**, 124103.

Simon, M., Reznikova, E., Nazmov, V., Grund, T. & Last, A. (2010). *AIP Conf. Proc.* **1221**, 85–90.

Simon, R., Buth, G. & Hagelstein, M. (2003). *Nucl. Instrum. Methods Phys. Res. B*, **199**, 554–558.

Snigirev, A., Kohn, V., Snigireva, I. & Lengeler, B. (1996). *Nature (London)*, **384**, 49–51.

Snigirev, A. & Snigireva, I. (2008). In *Modern Development in X-ray and Neutron Optics, Springer Series in Optical Sciences*, Vol. 137, pp. 255–285. Heidelberg: Springer Verlag.

Vaughan, G. B. M., Wright, J. P., Bytchkov, A., Rossat, M., Gleyzolle, H., Snigireva, I. & Snigirev, A. (2011). *J. Synchrotron Rad.* **18**, 125–133.

Vogt, H., Simon, M., Last, A., Marschall, F., Mohr, J., Nazmov, V., Eisenhower, R. & Mettendorf, K. U. (2011). *Proc. SPIE*, **8167**, 81670V.

Welnak, C., Chen, G. J. & Cerrina, F. (1994). *Nucl. Instrum. Methods Phys. Res. B*, **347**, 344–347.